Ray Systems and Craters Generated by the Impact of Nonspherical Projectiles

F. Pacheco-Vázquez*
Instituto de Física, Benemérita Universidad Autónoma de Puebla, Apartado Postal J-48, Puebla 72570, Mexico

(Received 31 October 2018; published 26 April 2019)

The impact of a spherical projectile on an evened-out granular bed generates a uniform ejecta of material and a crater with a raised circular rim. Recently, Sabuwala *et al.* [Phys. Rev. Lett. **120**, 264501 (2018)] found that the uniform blanket of ejecta changes to a set of radial streaks when a spherical body impacts on an undulated granular surface, being a plausible explanation to the enigmatic ray systems on planetary bodies. Here, we show that ray systems can also be generated by the impact of nonspherical projectiles on a flat granular surface. This is a reasonable explanation considering that meteorites are rarely spherical. Moreover, by impacting bodies of different geometries, we show that the crater size follows the same power-law scaling with the impact energy found for spherical projectiles, and the crater rim becomes circular as the impact energy is increased regardless of the projectile shape, which helps to understand why most impact craters in nature are rounded.

DOI: 10.1103/PhysRevLett.122.164501

Craters observed on Earth and other celestial bodies have different origins including meteorite impacts, volcanic eruptions, explosions, and subsidence [1,2]. Low-energy laboratory experiments with granular materials mimicking such mechanisms have been of great relevance to disclose different cratering features [3–12]. Impact experiments are usually carried out by dropping spherical projectiles, solid [3–7] or granular [8], against a flattened granular bed. The impact ejects a uniform curtain of material [13] and leaves a circular depression (bowl shaped or with central uplifts). Crater morphologies obtained by this method are found to be very similar to those observed on planetary surfaces [3,14–16]; however, one feature remained a mystery for decades [17]: ejecta rays, radial streaks of fine ejecta thrown out from the impact site. These ejections are called ray systems, and two examples are those surrounding the lunar craters Copernicus and Tycho. A great advance in understanding the origin of ray systems was reported very recently [18], when ejecta rays were produced by impacting a sphere on a surface with undulations. The number of rays was found to be directly proportional to the projectile diameter and inversely proportional to the undulation wavelength.

Surface undulations appear to be a required condition for the formation of ray systems, revealing the importance of considering the impacted surface topography in cratering studies. Another aspect rarely considered is that meteorites are not perfect spheres. In this Letter, we report that ejecta rays can also be generated when a flat granular bed is impacted by nonspherical projectiles. Balls with protuberances, amorphous meteoritelike projectiles, and other bodies with different cross section geometries (square, triangular, circular, and star shaped) were dropped from a given height h ($0.1\ \text{m} \leq h \leq 5.1\ \text{m}$) into a bed of 120 kg of sand (density $\rho_s = 2.66\ \text{g/cm}^3$ and grain size d_g in the range 150–250 μm), see details in [19]. It was found that rays emerge from the curved zones of the projectile surface that make the ejected material converge and be redirected in a single direction. An analysis based on geometry and momentum considerations was used to explain the number of ejected rays and their orientation. The temporal evolution of the ejecta and its dimensions as a function of the impact energy were also investigated. On the other hand, by measuring circularity, we show that the crater rim becomes circular as the impact energy increases regardless of the projectile shape, and the crater diameter follows the well-known 1/4-power law of the impact energy obtained for perfect spheres. Our results indicate that a crater depression brings scarce information about the original meteorite shape, but more insight can be deducted from the distribution of the ejected material.

Ray systems.—Let us first analyze the ejecta patterns produced by impacts of projectiles with a different number of protuberances N_p. Each projectile consisted of a modeling clay ball of radius $R = 22.5$ mm with 2 to 16 steel hemispherical protrusions of radius $r = 3.95$ mm equally separated along one ball circumference. The projectiles were dropped from $h = 185$ cm and filmed at 2000 fps. Snapshots in Fig. 1(a) show the impact of a projectile with 12 protrusions generates 12 rays. This pattern clearly contrasts with the continuous corona produced by the ball without protuberances shown in Fig. 1(b); see also videos in the Supplemental Material [19]. At first glance, since the number of rays N_r is equal to N_p, one could suppose that one ray is ejected by each protuberance. Nevertheless, experiments with $N_p = 2,\ 4,\ 8$ produce $N_r = 4,\ 8,\ 16$, respectively; see Figs. 1(c)–1(e). Indeed,

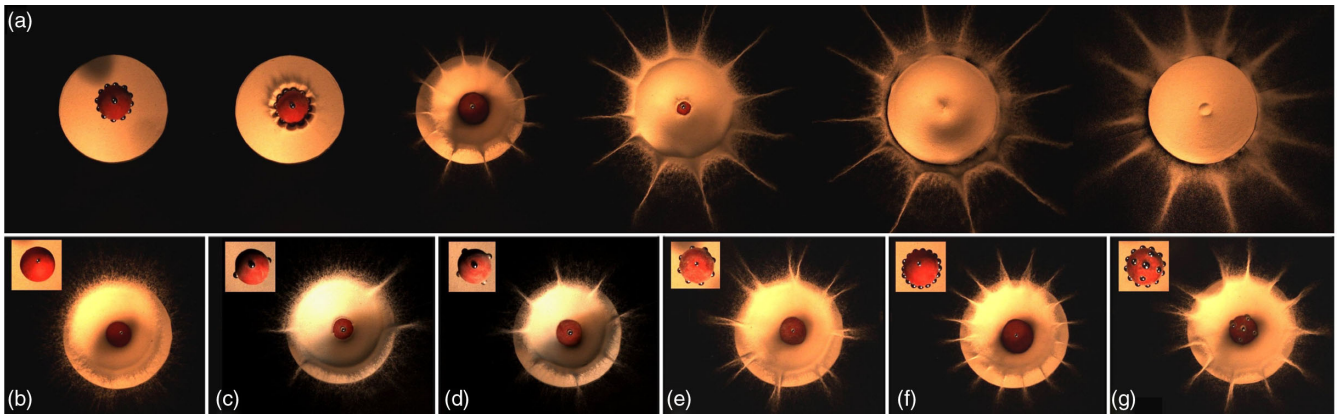

FIG. 1. (a) Snapshots showing ejecta rays produced by the impact of a projectile with $N_p = 12$ protuberances. (b) For a smooth projectile, i.e., $N_p = 0$, the number of rays $N_r = 0$. (c)–(f) For $N_p = 2, 4, 8$ one gets $N_r = 4, 8, 16$, respectively; however, for $N_p = 16$, $N_r = 16$ since adjacent rays converge into one. (g) A projectile with 22 protuberances produces 12 rays, equal to the number of protuberances along its circumference. See complete sequences in [19].

each protrusion generates two rays. For the case $N_p = 8$, the rays are very close to each other. For larger values of N_P, two rays converge into a single one, and that is the reason why $N_r = N_P$ for 12 and 16 protuberances in Figs. 1(a) and 1(f), respectively. We also performed experiments with $N_p = 22$ protuberances distributed on the entire sphere surface; see Fig. 1(g). As can be seen, $N_r = 12$, which coincides with the number of protuberances distributed along the circumference parallel to the bed at the impact. Thus, the shape of this cross section is what determines the final ejecta distribution.

In order to understand what defines the number of rays and how they are formed, let us consider the diagram shown in Fig. 2(a). The fact that a spherical projectile forms a corona that spreads radially [as in Fig. 1(b)] is a clear indication that the material is always ejected with a horizontal velocity component v_h pointing towards the direction $\hat{\boldsymbol{n}}$ normal to the projectile surface. For the case of a sphere with protuberances, some of the material ejected by the lumps provides momentum in the tangential direction $\hat{\boldsymbol{t}}$ when it collides with the radial ejection produced by the sphere [see Fig. 2(a)]. This generates two rays deviated at an angle θ from $\hat{\boldsymbol{n}}$ at the two points where each lump intersects the sphere and the bed surface, which explains the relation $N_r = 2N_p$. However, the deviation θ from $\hat{\boldsymbol{n}}$ implies that if the separation S between two adjacent lumps is small the rays emerging between them can converge forming a single one, see Fig. 2(b); in such cases $N_r = N_p$. We figured out that this happens when S is of the order of the protuberance size $2r$. Since the protrusions are equally separated, the arch length $S \approx (2\pi R/N_p) - 2r$. Equating this relation with $2r$, one estimates that adjacent rays start to merge when $N_p = N_p^* \approx (\pi R/2r)$. For $R = 22.5$ mm and $r = 3.95$ mm, one finds $N_P^* \sim 9$. Below this value $N_r = 2N_p$, and for $N_p > N_p^*$ one gets $N_r = N_p$, which coincides with our observations. The above condition was confirmed for different aspect ratios r/R. Additionally, assuming that the sphere provides to the grains a normal momentum $\vec{p}_n = \rho_l R v_h \hat{n}$ and the lump a tangential momentum $\vec{p}_t = \rho_l r v_h \hat{t}$, where ρ_l is the mass of grains per unit length ejected radially from each body, one obtains that $\theta \sim (\pi/2) - \arctan(R/r)$. This relation satisfies the following required conditions: if $r \ll R$, $\arctan(R/r) \to (\pi/2)$ and $\theta \approx 0$, which means that the grains are ejected radially ignoring the presence of the protuberance. If $r = R$, $\arctan(R/r) = \pi/4$ and $\theta \approx 45°$. This condition can be applied, for instance, to the case of two

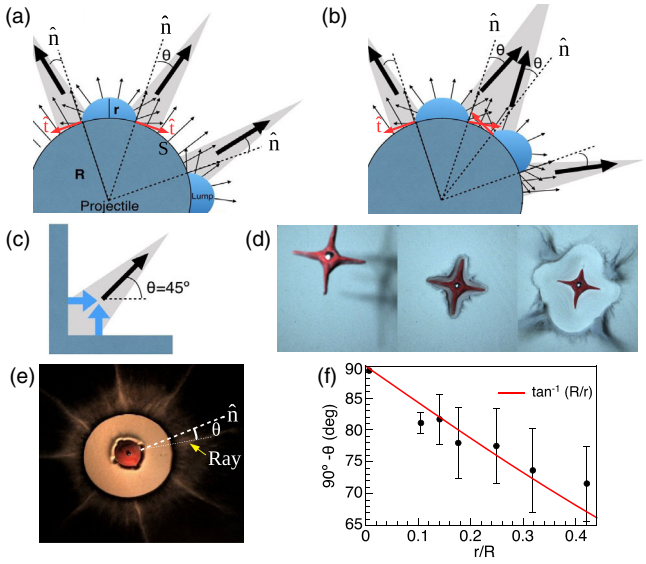

FIG. 2. Sketches of ray formation: (a) each lump of radius r embedded on a spherical projectile of radius R generates two rays. (b) If the lumps are close, the individual rays converge into a larger one. (c) Equal perpendicular walls generate an ejection at 45°. (d) Snapshots showing rays expelled at 45° during the impact of a star-shaped projectile. (e) Deviation θ of a ray from the radial direction $\hat{n}$. (f) (90°–θ) vs r/R.

perpendicular identical walls shown in Fig. 2(c). Since each wall contributes with the same momentum, the ray must be ejected at 45°. Snapshots in Fig. 2(d) showing the impact of a star-shaped projectile confirm our expectations (see video in the Supplemental Material [19]). We measured θ vs r/R from the ray's patterns as it is indicated in Fig. 2(e). The results reported in Fig. 2(f) (black points) are well described by the dependence on $\arctan(R/r)$ given above (red line).

Let us now quantify the ejecta dimensions in function of the impact height. Figure 3(a) depicts how we measured the maximum ray length L_{rays}, the maximum ray height H_{rays}, the ejecta curtain radius R_{curt}, and the ejecta angle α when the curtain reaches its maximum height H_{curt}. Using the projectile shown in Fig. 1(a) ($m = 103.6$ g, $R = 22.5$ mm, and $r = 3.95$ mm) dropped from $h = 26$–512 cm (i.e., kinetic energy at the impact $\text{KE}_0 = 0.4$–5.2 J), we found that $\alpha \approx 47° \pm 2°$ independently of KE_0, similar to the results found using spheres in [13,22]. Figure 3(b) shows that the ejecta expands at early times as $R_{\text{curt}} - R \sim t^{0.62}$, where t is the time from the moment at which the ejecta starts to appear; however, after $t = 0.1$ s, the ejecta curtain grows almost at constant speed. These two regimes were also observed in [13]. Regarding H_{rays} and H_{curt}, Fig. 3(c) shows that both obey a power-law $H_{\text{max}} \propto h^{0.73}$, which remarkably leads us to $H_{\text{rays}}/H_{\text{curt}} \approx 1.6$ for all values of KE_0.

The most difficult parameter to quantify was L_{rays} due to the dispersion of grains during the flight. The horizontal range for

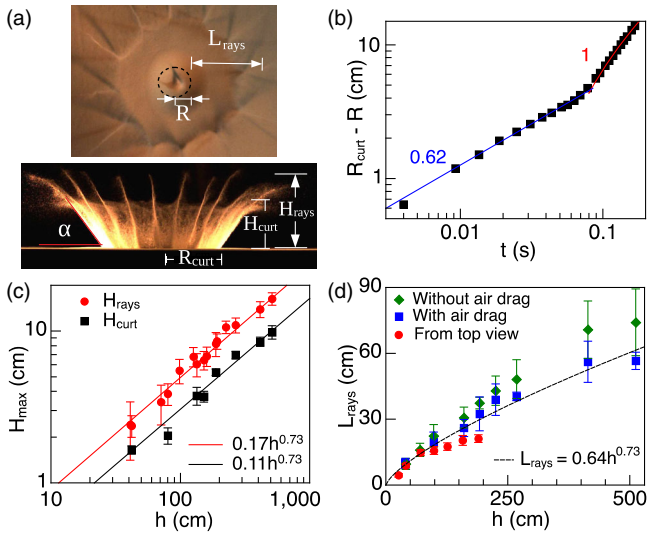

FIG. 3. (a) Top and lateral views of the ejecta indicating the measured parameters L_{rays}, α, R_{curt}, H_{rays}, and H_{curt}. (b) Log-log plot of $(R_{\text{curt}} - R)$ vs time t. (c) Log-log plot of H_{max} for the rays and the curtain as a function of the drop height h. In both cases $H_{\text{max}} \propto h^{0.73}$ (solid lines). (d) L_{rays} vs h measured from top videos (circle) and estimated considering (diamond)/neglecting (rectangle) air drag. The dashed line corresponds to $L_{\text{rays}} = (0.64 \pm 0.01)h^{0.73\pm0.01}$ derived from the power-law dependence of H_{rays}. Power laws have been widely used to describe the ejecta dynamics for low-speed and hypervelocity impacts [13,22,23].

grains ejected with velocity v and angle α in a parabolic flight is given by the ballistic equation $\Re = v^2 \sin(2\alpha)/g$. Since $(v \sin\alpha)^2 = 2gH_{\text{max}}$ and for the rays $H_{\text{max}} \approx 0.17h^{0.73}$, one finds $L_{\text{rays}} \sim \Re = 4H_{\text{max}}/\tan\alpha \approx 0.64h^{0.73}$. This expression was plotted in Fig. 3(d) (−) and compared with direct top view measurements (circle) only for $h < 200$ cm due to experimental setup limitations. To surpass this restriction, we tracked the tips of individual rays at early times of the ejection for $h = 26$–512 cm (see details in [19]). By fitting the trajectories with equations of motion, we estimated L_{rays} vs h neglecting and including air drag, see Fig. 3(d). Note that the ballistic equation and the estimated values with air drag follow a very similar trend. This should not surprise us since the inclusion of the power-law dependence of H_{max} in the ballistic equation takes into account the energy dissipated during the impact and also the air drag during the ascending flight. According to Refs. [13,24], the velocity of an ejected grain is appreciably reduced by air drag over a distance $L_{\text{drag}} = 4d_g\rho_s/6\rho_{\text{air}}$ during which the grain encounters its own mass (where ρ_{air} is the air density). In our case, $L_{\text{drag}} \geq 22$ cm for the finest grains ($d_g \approx 150$ μm). Thus, the air resistance cannot be neglected for long rays. Moreover, ray fragmentation into granular clusters [25,26] was observed during long flights. The clusters at the tip and the fastest grains fall apart from the continuous jet and cannot be easily visualized from the videos; for that reason, we measured smaller lengths than the real ones.

Ray systems generated by meteoritelike projectiles.— The previous results were obtained using spherical projectiles with protuberances symmetrically distributed. Nonetheless, real meteorites are irregular in shape and shallow pits (regmaglypts) may be seen on some parts of the surface. Inspired by this, we performed experiments using amorphous projectiles with marked curvatures and pits. A projectile with shallow pits does not produce rays [Fig. 4(a)]. In contrast, an irregular projectile generates rays emerging from the most concave curvatures of its surface [Fig. 4(b) and video in the Supplemental Material

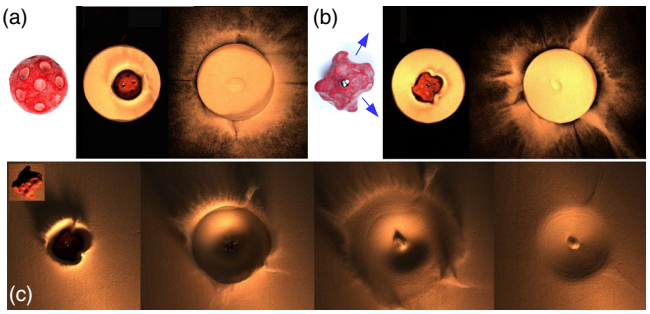

FIG. 4. (a) Uniform ejection produced by a ball with shallow pits. (b) Rays generated by the impact of an irregular projectile with concave curvatures of its surface (the arrows indicate the expected direction of the main rays). (c) Crater with circular rim and two rays produced by the irregular projectile.

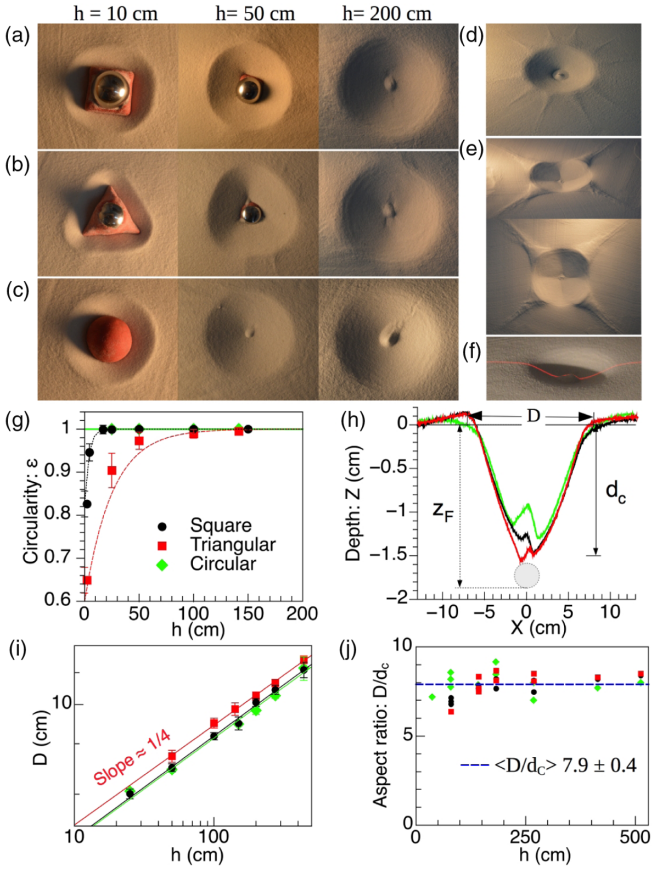

FIG. 5. (a)–(c) Pictures of craters produced by projectiles of (a) square, (b) triangular, and (c) circular cross sections impacting from different drop heights h. In the three cases $m = 76.6$ g. (d), (e) Different views of craters produced by (d) a projectile with 12 protrusions and (e) a star-shaped projectile released from $h = 400$ cm (the ejected rays are also visible). (f) Laser profilometry used to determine the crater profiles. A similar technique was used in Refs. [6,11]. (g) Crater circularity ϵ as a function of h for the three projectile geometries. (h) Example of X, Z profiles obtained from the laser profilometry. D and d_c are the crater diameter and depth, respectively, and Z_f is the final penetration depth of the projectile. (i) Log-log plot of D vs h for the three geometries shown in (a)–(c); $D \sim h^{1/4}$ in all cases. (j) Crater aspect ratio D/d_c vs h for the three geometries [same color-symbol code from (g)–(j)].

[19]]. From this observation, we speculate that, possibly, some planetary ray systems were generated by the impact of meteorites with marked concave curvatures. Furthermore, some clues about the meteorite shape can be derived from the final distribution of rays.

Crater morphology.—So far, we have focused our discussion on ray systems. Another remarkable aspect noticed in Fig. 4(c) is that the final crater has a circular rim regardless of the irregular shape of the impactor. Figures 5(a)–5(c) show pictures of craters produced by projectiles of different cross section geometries (square, triangular, and circular). For $h = 10$ cm, the final crater preserves some information about the projectile shape. Nevertheless, as the impact height increases, the crater becomes circular. Something similar happens with the projectile of 12 protuberances and the star-shaped projectile [Figs. 5(d) and 5(e)]. In order to quantify the crater roundness, we measured the circularity ϵ of the crater rims using the software IMAGEJ [27]. Figure 5(g) shows ϵ vs h for the three cases shown in Figs. 5(a)–5(c). For the circular projectile $\epsilon = 1$, as expected. For the square and triangular cross sections $\epsilon(h = 0) = \epsilon_0 \approx 0.82$ and 0.65, respectively, and these values grow rapidly to $\epsilon \approx 1$ as h increases. This growth is well fitted by the exponential saturation $\epsilon = 1 - (1 - \epsilon_0)e^{-h/h^*}$ (dashed lines), where h^* is a fitting parameter dependent on the projectile geometry. For $h > 200$ cm, one cannot guess the possible shape of the impactor from the crater morphology since for all cases the crater rim is circular ($\epsilon = 1$). A similar phenomenon was observed with craters produced by the collapse of pressurized cavities in a granular bed [9]: for deep cavities, the resulting crater becomes circular independently of the initial cavity shape due to material rearrangement by avalanches during the collapse. Therefore, the crater roundness in our case can be associated with the fact that the excavation energy augments when the impact height increases, creating deeper cavities and enabling the rearrangement of material.

Finally, we obtained the crater profiles using a laser line as shown in Fig. 5(f). Examples of these profiles shown in Fig. 5(h) for the three projectile geometries reveal craters of a very similar size. From the profiles, we obtained the crater diameter D and its depth d_c as a function of h. The log-log plot in Fig. 5(i) indicates that D follows a power-law dependence of the form $D = Ch^p$. The best fit of the experimental data gives the following for each case: $D_{\text{square}} = (2.60 \pm 0.11)h^{0.254\pm0.008}$ (black line), $D_{\text{triangular}} = (2.84 \pm 0.09)h^{0.248\pm0.006}$ (red line), and $D_{\text{circular}} = (2.59 \pm 0.18)h^{0.252\pm0.013}$ (green line). Therefore, the well-known $1/4$-power dependence on energy for spherical projectiles [3,4,8] is also valid for nonspherical impactors. We also found for the three geometries a nearly constant crater aspect ratio $D/d_c \approx 8$ [Fig. 5(j)] close to the value reported in Ref. [3] for impacts of spheres. Although analyzing the final depth Z_F reached by the projectile is out of the aims of this Letter, our data in the Supplemental Material [19] indicate a scaling close to $Z_F \propto h^{1/2}$ instead of the $1/3$-power dependence reported in Ref. [4], which could be associated with differences in energy scales. This aspect will be studied in detail in a forthcoming investigation.

Conclusions.—We have shown for the first time that ray systems can be produced by nonspherical projectiles impacting on a flat granular bed. Our results, together with those reported recently in Ref. [18], make clear that ray systems appear if the interface between the projectile contour and the granular surface has a shape that provides nonradial horizontal momentum to the grains and makes

them converge in a fine ejecta. Therefore, considering the projectile silhouette and the topography of the impacted bed is fundamental to describe the ray systems geometry. On the other hand, by studying the crater morphology, we found that the crater dimensions follow the same power-law dependence on the impact energy found for spherical projectiles. Even more remarkable is that the crater contour becomes circular independently of the projectile shape as the impact energy increases, and this helps to understand why most impact craters observed in nature have circular rims regardless the irregular shape of meteorites.

This research was supported by CONACYT Mexico through the Grant No. CB-0242085 and VIEP-BUAP Project No. ID-100522743.

*Corresponding author.
fpacheco@ifuap.buap.mx

[1] H. J. Melosh, *Impact Cratering: A Geologic Process* (Oxford University Press, New York, 1989), Vol. 11.
[2] R. G. Andrews, J. D. L. White, T. Durig, and B. Zimanowski, J. Geol. Soc. **173**, 265 (2016).
[3] A. M. Walsh, K. E. Holloway, P. Habdas, and J. R. de Bruyn, Phys. Rev. Lett. **91**, 104301 (2003).
[4] J. S. Uehara, M. A. Ambroso, R. P. Ojha, and D. J. Durian, Phys. Rev. Lett. **90**, 194301 (2003).
[5] S. J. de Vet and J. R. de Bruyn, Phys. Rev. E **76**, 041306 (2007).
[6] P. Umbanhowar and D. I. Goldman, Phys. Rev. E **82**, 010301(R) (2010).
[7] K. Hayashi and I. Sumita, Icarus **291**, 160 (2017).
[8] F. Pacheco-Vázquez and J. C. Ruiz-Suárez, Phys. Rev. Lett. **107**, 218001 (2011).
[9] F. E. Loranca-Ramos, J. L. Carrillo-Estrada, and F. Pacheco-Vázquez, Phys. Rev. Lett. **115**, 028001 (2015).
[10] R. Bartali, Y. Nahmad-Molinari, and G. M. Rodríguez-Linán, Earth Moon Planets **116**, 115 (2015).
[11] F. Pacheco-Vázquez, A. Tacumá, and J. O. Marston, Phys. Rev. E **96**, 032904 (2017).
[12] M. Gao, X. Liu, L. P. Vanin, T. Sun, X. Cheng, and L. Gordillo, AIChE J. **64**, 2972 (2018).
[13] J. O. Marston, E. Q. Li, and S. T. Thoroddsen, J. Fluid Mech. **704**, 5 (2012).
[14] J. C. Ruiz-Suarez, Rep. Prog. Phys. **76**, 066601 (2013).
[15] H. Katsuragi, *Physics of Soft Impact and Cratering* (Springer, Japan, 2016).
[16] D. Van der Meer, Annu. Rev. Fluid Mech. **49**, 463 (2017).
[17] J. R. de Bruyn, Physics **11**, 64 (2018).
[18] T. Sabuwala, C. Butcher, G. Gioia, and P. Chakraborty, Phys. Rev. Lett. **120**, 264501 (2018).
[19] See Supplemental Material at http://link.aps.org/supplemental/10.1103/PhysRevLett.122.164501 for more information about methods, particle tracking, and analysis of grain trajectories considering air drag. Find also there the analysis of data about the final penetration depth reached by projectiles of different geometries depending on the impact energy, as well as videos about the impact of projectiles with different geometries. Included in the Supplemental Material are Refs. [20,21].
[20] Z. Wang, S. Ren, and N. Huang, PLoS One **9**, e105208 (2014).
[21] L. A. López-Rodríguez and F. Pacheco-Vázquez, Phys. Rev. E **96**, 030901(R) (2017).
[22] S. Deboeuf, P. Gondret, and M. Rabaud, Phys. Rev. E **79**, 041306 (2009).
[23] K. R. Housen and K. A. Holsapple, Icarus **211**, 856 (2011).
[24] W. K. Hartmann, Icarus **63**, 69 (1985).
[25] J. R. Royer, D. J. Evans, L. Oyarte, Q. Guo, E. Kapit, M. E. Möbius, S. R. Waitukaitis, and H. M. Jaeger Nature (London) **459**, 1110 (2009).
[26] G. Caballero, R. Bergmann, D. van der Meer, A. Prosperetti, and D. Lohse, Phys. Rev. Lett. **99**, 018001 (2007).
[27] IMAGEJ is an open source Java image processing program inspired by NIH Image.